Energy balance and mixing between waves and eddies in stably stratified turbulence

H. Lam, A. Delache, F S Godeferd

Energy balance and mixing between waves and eddies in stably stratified turbulence

H. Lam[1]†, A. Delache[1,2] and F. S. Godeferd[1]

[1]Laboratoire de Mécanique des Fluides et d'Acoustique, Univ Lyon, École centrale de Lyon, INSA Lyon, Université Claude Bernard Lyon I, CNRS, France

[2]Laboratoire de Mécanique des Fluides et d'Acoustique, Univ Lyon, site de Saint-Étienne, Université Jean Monnet de Saint-Étienne, CNRS, France

(Received xx; revised xx; accepted xx)

DNS simulations of stably stratified turbulence explore the strong stratification regime and the transition between the viscosity-affected stratified and the strongly stratified regimes. The 3D field is decomposed into Internal Gravity Waves (IGW) and eddy motion by using an extended Riley decomposition (Riley *et al.* 1981) that takes into account the space-time properties of waves, their modification by vertically sheared horizontal flow and the vertical mixing by eddies (Lam *et al.* 2020). We establish the evolution equations for the IGW and eddy parts separately. Up to buoyancy Reynolds number $Re_b \sim 1$, we observe that eddy dissipation is larger than IGW dissipation and is reinforced by an additional exchange that pumps energy from IGW to eddy. For higher Re_b, the two dynamics seems to be separate and no global exchange is observed. The origin of the mixing coefficient in terms of IGW and eddy is computed. At the largest Re_b considered, the mixing due to eddies is four times the mixing due to waves.

Key words: In line

1. Introduction

In stably stratified turbulence, Internal Gravity Waves (IGW) and eddies are closely entangled and interact with each other at different scales, as in the ocean. Many studies are focused on each type of interaction separately. The wave-vortex interaction studied the propagation of IGW through large quasi-geostrophic eddy flow (Müller 1976) where a transfer of energy from eddy to waves is achieved. The eddies appear as a trap to deviate the ray of IGW (Moulin & Flór 2006). The wave-wave interaction was studied from triad interactions (Olbers 1976) to a stochastic field composed of many resonant triadic interactions by Müller *et al.* (1986) and extended by the formalism of wave turbulence by Lvov *et al.* (2010). The creation of IGWs in a surrounding quiescent region due to a localized stratified turbulent cloud has been studied by Maffioli *et al.* (2014). Lelong & Riley (1991) studied the weakly non-linear interactions in a highly stratified system between a vortical mode (i.e. a horizontal rotating eddy) and an IGW. They show that the vortical mode acts as a catalyst and facilitates energy transfer between the waves. Nevertheless, in stably stratified turbulence, mixing

† Email address for correspondence: henri.lam@ec-lyon.fr

by waves and eddies therefore occurs over a wide range of scales, rendering difficult their separation and precise identification of mutual interactions. According to Brethouwer *et al.* (2007), several regimes of stratified turbulence are found depending on the Froude number $Fr = \varepsilon_u/Nu_h^2$ and the buoyancy Reynolds number $Re_b = \varepsilon_u/\nu N^2$ where ε_u is the kinetic energy dissipation, u_h is the rms horizontal velocity, N the Brunt-Väisälä frequency and ν the viscosity. For a strong stratification, at $Fr \ll 1$ and $Re_b \ll 1$, the regime is a viscosity-affected stratified flow (VASF) and the flow is dominated by a large, smooth and stable horizontal layers and few turbulent-like structures, such as vortex tubes, are observed. This flow appears to be characteristic of a large-scale vortical mode (Waite & Bartello 2004). At $Fr \ll 1$ and $Re_b \gg 1$, the regime is strongly stratified turbulence (SST) where large vertically sheared horizontal flow (VSHF) and three-dimensional (3D) overturning structures are observed. In order to separate a turbulent field into eddy and wave parts, Riley *et al.* (1981) first proposed a 3D spatial decomposition. This decomposition was extensively used for stably stratified flow with or without rotation in many theoretical and numerical studies that explored different properties of IGW, eddies, VSHF and their interactions in terms of energy, transfer and scale dependence (see *e.g.* Godeferd & Cambon (1994), Bartello (1995), Smith & Waleffe (2002), Kimura & Herring (2012), Herbert *et al.* (2016)). This approach appears to be relevant at small Froude number $Fr \ll 1$ and low buoyancy Reynolds number $Re_b \ll 1$ where the eddies are mostly horizontal and the vertical motion and density field are associated to IGW (Lelong & Riley 1991). Nevertheless, when Re_b increases, as in the SST regime, a part of the vertical velocity and density fields are linked to vertical mixing and therefore not to waves. Moreover, IGW are characterized by their dispersion relation $\omega_r(\mathbf{k}) = N\cos\theta(\mathbf{k})$ where $\theta(\mathbf{k})$ is the angle of the wave vector $\mathbf{k}$ with the horizontal plane. Clearly, the Riley decomposition is a spatial decomposition and does not reflect the temporal properties of the waves by including all frequencies of the flow motion, even outside of the dispersion relation. Therefore, the dispersion relation of IGW can not be characterized with this decomposition.

Alternative approaches have been developed, for example by selecting only a few Fourier modes (Lindborg & Brethouwer 2007), and detecting in their temporal signal the presence of frequency peaks linked to their wave vector by the dispersion relation, which is a signature of IGW. Recent detailed analyses have been proposed to study waves in turbulent flow: in stratified turbulence, a global signature of IGW was observed in experiments of Savaro *et al.* (2020) and in numerical simulations by Di Leoni & Mininni (2015), and Maffioli *et al.* (2020) clearly characterized the presence of IGW by using a temporal analysis of reduced energy from the Riley decomposition.

Nevertheless, there is a heavy computational cost to a complete wave/eddy separation, so that simplifying assumptions are used in the above-mentioned methods: horizontal isotropy, and the fact that transport of IGW occurs in a homogeneous distribution of VSHF. The latter assumption discards possible variations in time and space of the transporting motion that in principle modifies significantly the waves dispersion relation. Recently, Lam *et al.* (2020) have extended the Riley decomposition by taking into account the 3D spatial and temporal properties of fields. This method permits to extract the 3D fields of IGW and eddies separately, accounting for the overturning of density and vertical velocity. It is based on a joint analysis in space and time by performing the full 4D Fourier transform. This is computationally expensive and requires adequate

numerical resolution in time and in space. In this article, we use a more advanced and versatile version of this method which also takes into account the spatial and temporal variation of the VSHF on the dispersion relation. Nevertheless, in order to achieve statistical stationarity of the flow, the VSHF is damped in our DNS but it plays a significant role even if it does not dominate the overall structure of the flow. It is then possible to obtain a precise budget of wave and vortex energies, their interactions and the different fluxes. Thanks to this budget, it becomes possible to clearly decompose the mixing coefficient Γ used in oceanography to model vertical turbulent mixing (Mashayek *et al.* 2017; Ivey *et al.* 2008), into a part coming from the waves and another part coming from the eddies. In order to improve modelling, it is possible to analyse the mixing done by eddies due mostly to the breaking of IGW (MacKinnon 2017) and the mixing by IGW themselves.

2. Extraction of eddies and waves in stratified turbulence

2.1. *Governing equation*

We consider a linearly stratified incompressible fluid, and the corresponding Navier-Stokes equation under the Boussinesq approximation:

$$\partial_t \mathbf{u} + \boldsymbol{\omega} \times \mathbf{u} + \nabla p - \nu \nabla^2 \mathbf{u} = b\mathbf{z} + \mathbf{F_u} \tag{2.1}$$

$$\partial_t b + \mathbf{u} \cdot \nabla b - \mathcal{X} \nabla^2 b = -N^2 u_z \ . \tag{2.2}$$

The velocity vector is $\mathbf{u} = (u_x, u_y, u_z)$ with vorticity $\boldsymbol{\omega} = \nabla \times \mathbf{u}$, and p is the modified pressure field. The kinematic viscosity is ν and the thermal diffusivity $\mathcal{X}$. The Brunt-Väisälä frequency is N so that the buoyancy field b is the negative fluctuation of density around the mean constant gradient N^2. $\mathbf{z}$ is the unit vector of polar direction, also vertical. The flow can be set in motion via the body force $\mathbf{F_u}$. All equations and parameters are dimensionless by reference to length and scale

Our method for extracting the IGW from the full flow is based on the characteristics of the IGW. Indeed, classical IGW are plane-wave solutions of the inviscid equations, obtained by removing the non-linear terms of (2.1),(2.2), and identifying their dispersion relation $\omega_r(\mathbf{k})$. However, in the presence of large-scale advection (such as the VSHF), this dispersion relation $\omega_r(\mathbf{k})$ is modified. Indeed, taking into account only the sweeping effect of large structures with an advection velocity field $\mathbf{c}$ on the IGW, this modification of the IGW characteristics can be modelled by the following linearized equations:

$$\begin{aligned} \partial_t \mathbf{u}_G + \mathbf{c} \cdot \nabla \mathbf{u}_G + \nabla p_G - \nu_G \nabla^2 \mathbf{u}_G = b_G \mathbf{z} \\ \partial_t b_G + \mathbf{c} \cdot \nabla b_G - \mathcal{X}_G \nabla^2 b_G = -N^2 u_{z,G} + F_b \end{aligned} \tag{2.3}$$

and we shall use density forcing via F_b with new variables named $\mathbf{u}_G, b_G, \nu_G$ & $\mathcal{X}_G$ associated to equation (2.3). In our modeled of the modificaiton of IGW's characteristic, we do not take into account the refraction of waves by the vertical shear (*i.e.* $u_z \partial_z c$) as it does not change significantly our result. Indeed, in our DNS, we have $\partial_z c \sim 0.04 \ll N$ and the analytical result and preliminary numerical tests show that the dispersion relation is not deeply modified in this case with respect to the sweeping effect. The characteristics of the IGW are obtained by solving the equation (2.3) and are used to extract the wave part from the full velocity obtain by equation (2.2). In both cases , it is useful to use the same basis for equation (2.2) and (2.3). In Fourier space, incompressibility (velocity is perpendicular to

wave vector) suggests to introduce polar-spherical coordinates where the unit vectors of the so-called Craya-Herring frame are $(\mathbf{e}^t, \mathbf{e}^p, \mathbf{e}^k)$ defined with respect to the vertical axis $\mathbf{z}$:

$$\mathbf{e}^t = \frac{\mathbf{k}\times\mathbf{z}}{|\mathbf{k}\times\mathbf{z}|} \quad \& \quad \mathbf{e}^p = \frac{\mathbf{k}\times\mathbf{k}\times\mathbf{z}}{|\mathbf{k}\times\mathbf{k}\times\mathbf{z}|} \quad \& \quad \mathbf{e}^k = \mathbf{k}/k \tag{2.4}$$

Then the Fourier-transformed velocity is $\hat{\mathbf{u}}(\mathbf{k},t) = \hat{u}^t(\mathbf{k},t)\mathbf{e}^t + \hat{u}^p(\mathbf{k},t)\mathbf{e}^p + \hat{\mathbf{u}}^s(k_z,t)$ where $\hat{}$ represents the Fourier transform in space (details in Lam *et al.* (2020)). The toroidal part $\hat{u}^t$ is horizontal and correspond to a horizontal wave vector $k_h \neq 0$ with $k_h = (k_x^2 + k_y^2)^{1/2}$, and the poloidal part $\hat{u}^p$ contains both horizontal and vertical velocity and thus corresponds to IGW motion. In physical space, the corresponding velocity fields are u^t and u^p. Nevertheless, from this decomposition, we have excluded the VSHF mode noted in Fourier space $\hat{\mathbf{u}}^s(k_z,t) = \hat{\mathbf{u}}(k_h = 0, k_z, t)$ which corresponds to the horizontal velocity field with a purely vertical wave vector i.e. $k_h = 0$ and cannot be describe by the polar-spherical coordinates based on axis $\mathbf{z}$.

2.2. *Method of extraction*

In the original decomposition by Riley *et al.* (1981), the Craya-Herring frame is apply on velocity field in the limit of small Froude number, the poloidal part u^p is the velocity of IGW and the toroidal part u^t is the non-wave part which coincide with a two-dimensional horizontally rotational velocity associated to eddies dynamics and often called vortical mode. This decomposition appears to be relevant at low buoyancy Reynolds number $Re_b \ll 1$ and at low Froude number $Fr \ll 1$ where the flow is an interaction between vortical mode at large scale and IGW (see Lelong & Riley (1991)). But when Re_b increases, a part of vertical velocity u^p and of density b is linked to vertical mixing, and therefore not to waves. To account for this, Lam *et al.* (2020) extended the Riley's decomposition to explicitly include the space-time properties of waves and their transport by a constant advecting velocity $\mathbf{c}$ estimated from the energy of the VSHF.
In the case of a constant advection velocity $\mathbf{c}$, homogeneous in time and space, the Riley decomposition applied to (2.3) is rigorous. Indeed, an analytical solution of Green's function of the IGW could be obtained from the linearized equations (2.3) forced by Dirac functions in time and space $F_b = \delta(t)\delta(x)$. Solved in the four-dimensional Fourier domain in space and time $(\mathbf{k},\omega)$, and denoted $\tilde{}$. The Green's function of IGWs is composed only by the poloidal part denoted $\tilde{u}^p_{G,a}$ and by the density denoted $\tilde{b}_{G,a}$:

$$\begin{aligned}
\tilde{b}_{G,a}(\mathbf{k},\omega) &= \frac{1}{2}\left\{\left[\mathcal{X}k^2 + i(\omega+\omega_c^+(\mathbf{k}))\right]^{-1} + \left[\mathcal{X}k^2 + i(\omega-\omega_c^-(\mathbf{k}))\right]^{-1}\right\} \\
\tilde{u}^p_{G,a}(\mathbf{k},\omega) &= \frac{\mathrm{i}}{2N}\left\{\left[\nu k^2 + i(\omega+\omega_c^+(\mathbf{k}))\right]^{-1} - \left[\nu k^2 + i(\omega-\omega_c^-(\mathbf{k}))\right]^{-1}\right\}
\end{aligned} \tag{2.5}$$

where the analytical dispersion relation $\omega_c^{\pm}(\mathbf{k}) = \mathbf{c}\cdot\mathbf{k} \pm \omega_r(\mathbf{k})$ is ω_r modified to include $\mathbf{c}\cdot\mathbf{k}$ that represents the sweeping effect similar to Doppler shift. The toroidal part $\tilde{u}^t_{G,a}(\mathbf{k},\omega)$ is constant in time, i.e. with a zero frequency, and it is the vortical mode which is rotational horizontal flow i.e. $k_h \neq 0$ (see note 14 in Smith & Waleffe (1999)). Our new technique is based on a filter $\zeta(\mathbf{k},\omega)$ in four-dimensional space $(\mathbf{k},\omega)$ applied on the density field $\tilde{b}$ and velocity fied $\tilde{\mathbf{u}}$ from DNS. The wave part is obtained from the $\tilde{b}$ and $\tilde{\mathbf{u}}$ fields and by filtering the

frequencies ω associated with each wave vector $\mathbf{k}$ for the velocity component $\tilde{u}^p$ and density component $\tilde{b}$. In Lam *et al.* (2020), this filter is based on the analytical dispersion relation: $\zeta(\mathbf{k},\omega) = 1$ when $\omega = \omega_c^{\pm}(\mathbf{k})$ where $\mathbf{c}$ is horizontal and c varies between $[-c_V, c_V]$, c_V being the rms of VSHF amplitude. This supposes that the large sale such VSHF is modeled as a homogeneous flow that transports velocity fluctuations. In fact the velocity of VSHF vary along the z axis with time i.e. $\mathbf{c}(z,t)$ and it is not possible to derive an analytical solution such (2.5). More generally, no theoretical dispersion relation can be easily found when $\mathbf{c}$ is inhomogeneous. To overcome this difficulty we simulate directly the Green's function.

For a inhomogeneous advecting velocity $\mathbf{c}(z,t)$, we generalize a property that appears in the analytical wave solution (2.5): when the frequency $\omega \to \omega_c^{\pm}(\mathbf{k})$, the density energy $|\tilde{b}_G|^2$ peaks, only damped by viscosity. This permits to compute the Green's function of (2.3) where $\mathbf{c}(z,t)$ is the inhomogeneous VSHF, numerically extracted from DNS i.e. $\hat{\mathbf{c}}(k_z,t) = \hat{\mathbf{u}}(k_h = 0, k_z, t)$ and $F_b = \sum_{\mathbf{x},t} \delta(\mathbf{x})\delta(t)$ is an inhomogeneous distribution of Dirac functions in space and time. The extended filter is obtained by simply looking at the energy of $|\tilde{b}_G|^2$ with respect to the space variable $|\tilde{b}_G|^2$ and time variable ω. When the energy $\tilde{b}_G$ reaches a peak, for $(\mathbf{k}_0, \omega_0)$, we can define a wave by setting $\zeta(\mathbf{k}_0, \omega_0) = 1$. To reach the peak , the extended filter is therefore defined as:

$$\text{if } |\tilde{b}_G(\mathbf{k},\omega)|^2 \geqslant \beta^{-1}\text{max}_\omega|\tilde{b}_G(\mathbf{k},\omega)|^2 \text{ then } \zeta(\mathbf{k},\omega) = 1 \text{ else } \zeta(\mathbf{k},\omega) = 0 \qquad (2.6)$$

where the real parameter $\beta = 100$ is selected in order to capture all peaks of energy on a range of frequencies and take into account not only the spread of peak over frequencies due to diffusivity but inaccuracy due to spatial and temporal discretization (see section 3). The filter $\zeta(\mathbf{k},\omega)$ implicitly defines a new dispersion relation $\omega_G(\mathbf{k})$ that accounts for the inhomogeneity of $\mathbf{c}(z,t)$. It can be applied on the DNS fields to separates wave part ($\zeta = 1$, label 'w') from eddy part ($\zeta = 0$, label 'e'):

$$\begin{aligned} \tilde{\mathbf{u}}^w(\mathbf{k},\omega) &= \zeta(\mathbf{k},\omega)\tilde{u}^p(\mathbf{k},\omega)\mathbf{e}^p \\ \tilde{\mathbf{u}}^e(\mathbf{k},\omega) &= \tilde{u}^t(\mathbf{k},\omega)\mathbf{e}^t + (1-\zeta(\mathbf{k},\omega))\,\tilde{u}^p(\mathbf{k},\omega)\mathbf{e}^p \\ \tilde{b}^w(\mathbf{k},\omega) = \zeta(\mathbf{k},\omega)\tilde{b}(\mathbf{k},\omega) \;\text{ and }\; \tilde{b}^e(\mathbf{k},\omega) &= (1-\zeta(\mathbf{k},\omega))\,\tilde{b}(\mathbf{k},\omega)\ . \end{aligned} \qquad (2.7)$$

In this decomposition IGW are defined as being the poloidal and buoyancy components close to the dispersion relation. Eddies are defined here as elements that are not a wave as IGW and that are not the VSHF either. In this article, we speak of a eddy part for the convenience of the language. Indeed, we define the eddy part by what it is not. Nevertheless, the eddy part contains the mainly large-scale vortical mode which is a pure toroidal component up to the small-scale three-dimensional structures which are a mixture of poloidal and toroidal components.

The decomposition of $\tilde{\mathbf{u}}^w$ agrees with the observations of Maffioli *et al.* (2020) that only the poloidal components recover the waves dispersion relation. The wave part in (2.7) contains only frequencies corresponding to the dispersion relation and the eddy part contains a part of vertical velocity and the density. Applying the inverse four dimensional Fourier transform from frequency space $(\mathbf{k},\omega)$ to physical space $(\mathbf{x},t)$ *i.e.* $\mathbf{u}^a(\mathbf{x},t) = \sum_{\mathbf{k},\omega} \tilde{\mathbf{u}}^a(\mathbf{k},\omega)e^{-i\mathbf{k}\cdot\mathbf{x}-i\omega t}$, $b^a(\mathbf{x},t) = \sum_{\mathbf{k},\omega} \tilde{b}^a(\mathbf{k},\omega)e^{-i\mathbf{k}\cdot\mathbf{x}-i\omega t}$ (a stands for w, e and remaining part s), we obtain the

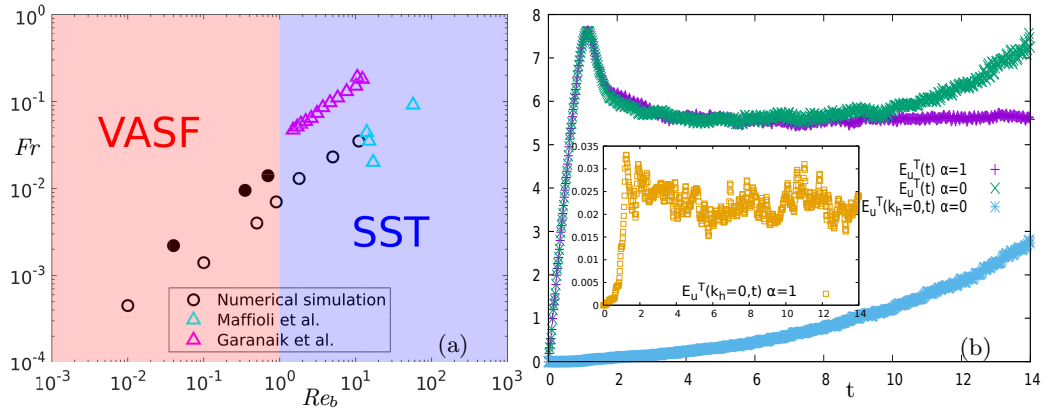

Figure 1: (a) Parameters of the numerical simulation done (empty circle is for 512^3 points and filed circle is for 256^3 points). For reference, the DNS of Maffioli *et al.* (2016) and Garanaik & Venayagamoorthy (2019) are shown (b) Total kinetic energy $E_u^T(t)$ and VSHF energy $E_u(k_h = 0, t)$ for $\alpha = 1$ and $\alpha = 0$ for $Re_b = 5$ and $Fr = 0.023$.

decomposition of velocity and density:

$$\mathbf{u}(\mathbf{x},t) = \mathbf{u}^w(\mathbf{x},t) + \mathbf{u}^e(\mathbf{x},t) + \mathbf{u}^s(\mathbf{x},t) \quad \text{and} \quad b(\mathbf{x},t) = b^w(\mathbf{x},t) + b^e(\mathbf{x},t)\ . \quad (2.8)$$

where the VSHF is a mean flow identified in physical space as $\mathbf{u}^s(\mathbf{x},t)$ and defined in Fourier space as $\hat{\mathbf{u}}^s(\mathbf{k},t) = \hat{\mathbf{u}}(k_h = 0, k_z, t)$.

This decomposition permits to define an orthogonal basis and an inner product in vector function space, by using the complete set of unit vector functions $e^{i\mathbf{k}\cdot\mathbf{x}}$ and $e^{i\omega t}$. For two functions $\hat{f}$ and $\hat{g}$, we thus define an inner product in terms of wave vector $\mathbf{k}$ and time t, as $[\hat{f}(\mathbf{k},t), \hat{g}(\mathbf{k}',t)] \equiv \frac{1}{T}\int_T \hat{f}(\mathbf{k},t)\overline{\hat{g}(\mathbf{k}',t)}\delta_{\mathbf{k}-\mathbf{k}'}\mathrm{d}t$ where T is the considered time span and $\bar{}$ is the complex conjugate. Due to the orthogonality of vector space functions and orthogonality of Fourier velocity with wave vector space $\mathbf{k}$ from incompressibility, one shows the orthogonality between wave, eddy, and shear parts: $[\hat{b}^i(\mathbf{k},t), \hat{b}^j(\mathbf{k}',t)] \neq 0$ and $[\hat{u}^i_m(\mathbf{k},t), \hat{u}^j_n(\mathbf{k}',t)] \neq 0$ only if $i = j$ and $\mathbf{k} = \mathbf{k}'$ (where i, j stand for w, e or s, and m, n stand for space direction x, y, or z). Moreover, the overall energetic content is $< \hat{f}, \hat{g} >= \sum_{\mathbf{k}} \Re[\hat{f}(\mathbf{k},t), \hat{g}(\mathbf{k},t)]$.

3. Numerical methodology and parameters

3.1. *Parameters space*

In a first type of DNS, equations (2.1) and (2.2) are solved using a standard pseudo-spectral algorithm in a 2π-periodic three-dimensional spatial domain. A phase shifting method is used to treat the non-linear term (see Lam *et al.* (2020) for details). The Prandtl number is $Pr = \nu/\mathcal{X} = 1$. Ten numerical simulations have been run with the parameters shown in table 1 for two resolution (256^3 and 512^3 points). The exploration of parameters is mainly based on 512^3 points, the lower resolution of 256^3 points is used to confirm and explore trends. We have plotted in Figure 1, the exploration points in the parameter space (Fr, Re_b) with some reference to Maffioli *et al.* (2016) and Garanaik & Venayagamoorthy (2019).

512^3 points with $\nu = 1/700$

N	Fr	Re_b	Re_h	Re_λ	D_E	$S_E(\%)$	$\omega_{\max}$	$\omega_{\min}$	$u_{rms}k_{max}$	$k_{max}\eta$	Δt $(\times 10^{-4})$
20	0.035	11	9000	146	760	0.3	1570	3	800	1.12	2
30	0.023	5	9500	148	1080	0.4	1570	3	810	1.12	2
50	0.013	1.8	10700	180	980	0.4	1570	3	890	1.12	2
70	0.007	0.9	18000	225	820	0.3	1570	3	990	1.12	2
100	0.004	0.5	31000	290	730	0.3	1570	3	1110	1.12	2
200	0.0014	0.1	51000	430	22	0.08	3140	6	1300	1.13	1
600	0.00045	0.01	49000	510	11	0.005	3140	6	1370	1.19	1

256^3 points with $\nu = 1/250$

N	Fr	Re_b	Re_h	Re_λ	D_E	$S_E(\%)$	$\omega_{\max}$	$\omega_{\min}$	$u_{rms}k_{max}$	$k_{max}\eta$	Δt $(\times 10^{-4})$
50	0.014	0.7	3600	94	2500	1	1570	3	423	1.18	4
70	0.0095	0.35	3900	109	420	0.16	1570	3	450	1.19	5
200	0.0022	0.04	8300	175	74	0.03	1570	3	557	1.21	4

Table 1: List of parameters in the seven DNS runs. $Re_h = u_h^4/(\varepsilon_u \nu)$ is the horizontal Reynolds number, S_E is the ratio of energy of shear flow over the total kinetic energy, D_E is the ratio of density of shear energy per point against the total kinetic energy per point, $\omega_{\max} = \frac{\pi}{\Delta t'}$ and $\omega_{\min} = \frac{2\pi}{T}$ are the the maximum and the minimum pulsation solved.

According to Brethouwer *et al.* (2007), our parameters explore a VASF regime which contains weak IGW interactions where wave anisotropy extends to small scales ($Fr \ll 1$ and $Re_b \ll 1$), as well as a SST regime where the scale of wave anisotropy is distinct from small dissipative scales ($Fr \ll 1$ and $Re_b \gg 1$). The exploration of those two regimes also induce a modification of the Taylor Reynolds number $Re_\lambda = u_{rms}\lambda/\nu$ with λ the Taylor scale and u_{rms} the rms velocity. The regimes studied in our numerical simulations and in other numerical simulation is shown in figure 1a. As shown in the figure, the two resolutions (points 256^3 and 512^3) explore different region of parameters space (Fr, Re_b) and we expect this to change the characteristic of the transition between the VASF and SST regime. They are few points in parameter space for a resolution of 256^3 points in order to explore a slight variation of Re_b and Fr. In fact the two parameters Fr and Re_b are dependent on each other i.e. $Re_b = Fr^2 Re_h$ through the horizontal Reynolds number $Re_h = u_h^4/(\varepsilon_u \nu)$ as defined by (Maffioli *et al.* 2016) and which accounts for the horizontal turbulence. The 256^3 simulations have almost one order of magnitude less Re_h than the 512^3 simulation (see table 1) for similar (Re_b, Fr). By playing with the resolution, one can study the dependence of the system either by fixing Fr and weakly increasing Re_b (from low to high resolution), or by fixing Re_b and weakly increasing Fr (from high to low resolution) in the parameter map.

3.2. *Numerical parameters*

The time step Δt varies with the stratification N to agree with the CFL condition. The spatial resolution is 512^3 points with maximum wavenumber $k_{\max} = 241$ such that $k_{\max}\eta \sim 1.1$, η being the Kolmogorov scale (see table 1). This moderate number of points is necessary because our wave/eddy decomposition requires

many 3D fields in time. Turbulence reaches a statistical stationary state due to the added body force F_u in equation (2.1), as in Maffioli *et al.* (2020) who injected a constant power $P = \int \mathbf{F_u} \cdot \mathbf{u} \, \mathrm{d}v = 10$. $\mathbf{F_u}$ is spectrally localized on a cylindrical envelope of horizontal wave number $k_h = 4$ and vertical wave number $1 \leqslant k_z \leqslant 3$, away from the VSHF at $\hat{\mathbf{u}}(k_h = 0, k_z)$. It forces the polodial and toroidal parts of the velocity equally. Thus this choice allows on average the wave and vortex components of the flow (in the sense of the Riley's decomposition) to be excited in equal proportions. The forced wavenumbers are at an angle θ_f where θ_f is the angle done by the wavevector $\mathbf{k}$ against the horizontal plane. It is forced in the range $0.72 \leqslant \theta_f \leqslant 1.31$, meaning that high frequencies close to N are forced and a wave turbulence cascade may develop with lower frequency. To delay the emergence of VSHF at large scale, we add a friction term $\hat{\mathbf{F}}_u - \alpha\hat{\mathbf{u}}(\mathbf{k}_h = 0, k_z)$ (with $\alpha = 1$) as proposed by Le Reun *et al.* (2017) to stabilise the geostrophic mode in rotating turbulence. The authors also note that this term mimics the effect of a horizontal wall. It also help the numerical simulation to reach a stationary state as shown in 1b. Indeed, we plot on figure 1b the total kinetic energy $E_u^T(t)$ and the kinetic energy of VSHF $E_u^T(k_h = 0, t)$ for $\alpha = 1$ and $\alpha = 0$. Both energies diverge when $\alpha = 0$ while those two kinetic energy converge when $\alpha = 1$ and this stationarity behavior allows to apply a time FFT with more accuracy. Furthermore the divergence of the kinetic energy $E_u^T(t)$ for $\alpha = 0$ is roughly the same as the divergence of the VSHF energy $E_u^T(k_h = 0, t)$ meaning that roughly the same amount of energy is advected by the VSHF. The mean difference between the two cases is that the flow is advected a lot by the VSHF in the first case ($\alpha = 0$) whereas in the damping case ($\alpha = 1$), the flow is less advected by the VSHF.

Our simulations contrast with those of Maffioli *et al.* (2020) in that we apply a friction term to quench VSHF to less than a few % of the total kinetic energy, though still active enough to contribute to the flow structuration. We show on table 1 that the percentage of shear energy over the total kinetic energy ($S_E = E_u^T(k_h = 0, t)/E_u^T(t)$) is very low. However, we still consider the VSHF to be the main advecting flow. Indeed, if we define the average density of shear kinetic energy of VSHF for each wave vector by $e_{\mathrm{shear}} = 0.5 \sum_z |\mathbf{u}_s(z)|^2/512$ (because the VSHF is characterised by $k_h = 0$ and $1 \leqslant k_z \leqslant 512$), and the average density of kinetic energy for each wave vector by $e_K = 0.5 \sum_{\mathbf{x}} |\mathbf{u}(\mathbf{x})|^2/512^3$, then we can define the average density ratio for each wave vector by $D_E = e_{\mathrm{shear}}/e_K$. The value D_E is given in table 1 and shows the relative importance of the VSHF compare to the number of points in the DNS involved. It shows that the VSHF importance per point is strong for weaker stratification ($D_E \sim 1000$) but decreases while still intense for higher stratification.

In a second type of DNS, to build the ζ function for the DNS with 512^3 points, the Green's function is simulated during $T = 10\ 000\Delta t$ by using equation (2.3) with the forcing term $F_b = \sum_{\mathbf{x},t} \delta(\mathbf{x})\delta(t)$ where each Dirac function is set at a random position and enforced at each time step Δt during the first $100\Delta t$. The initial condition of this calculation is zero. The velocity $\mathbf{c}$ comes from the VSHF $\hat{\mathbf{u}}(k_h = 0, kz)$ extracted every $\Delta t' = 10\Delta t$ from the DNS, after it has reached statistical stationarity. To ensure that IGW are not dissipated, the viscosity is chosen very small $\nu_G = \mathcal{X}_G = 10^{-8}$ and we check that only the poloidal part $\hat{u}^p$ and the density $\hat{b}$ are active with respect to the toroidal part $\hat{u}^t$ that is close to machine precision zero. We apply the FFT in time on 1000 fields of $\hat{b}_G$ extracted

every $\Delta t'$. For DNS with 256^3 points the time step Δt can be taken larger and result in a DNS with less iterations ($T = 4000$ *or* $5000\Delta t$) but with statistics written on the same time step $\Delta t' = 0.002$ as in numerical simulations with 512^3 points. The time step is chosen very small in order to capture the sweeping effect from the full rms velocity u_{rms} on the highest frequency of eddies $u_{rms}k_{max}$ as shown in a homogeneous and isotrope DNS simulation (Di Leoni *et al.* 2015). The highest frequency of eddies $u_{rms}k_{max}$ must be compare to maximum frequency ω_{max} and minimum frequency ω_{min}. The fields are not extracted at every Δt to reduce the memory cost and because in the DNS this time step is chosen to comply with the limit due to the CFL number.

The value $\beta = 100$ is based on the simulation of the Green's function under conditions similar to the analytical solution (2.5) for buoyancy $\tilde{b}_{G,a}$ which is a benchmark for our method. Indeed, two phenomena make imprecise the capture of peaks in the simulation of Green's functions. The first phenomenon comes from the effect of viscosity, even if it is very low (i.e. $\nu_G = \mathcal{X}_G = 10^{-8}$) the peaks spread out around the frequencies $\omega_c^{\pm}$ and this spreading is a pure physical process. For each wave vector $\mathbf{k}$, 100% of energy is localized on a single frequency $\omega_c^{\pm}(\mathbf{k})$ for analytical case whereas it is distributed over a bandwith of frequencies in simulation. The second problem is due to the time discretization: the frequency $\omega_c^{\pm}$ is not exactly measured, but is approximated by the two closest discrete frequencies. These two problems lead to a search for the set of points closest to the peak. When trying to capture the peak in a similar configuration to the analytical solution (2.5), we observe that the peaks span several orders of magnitude in amplitude over a bandwith of frequencies. In simulation, even if 100% of the energy is distributed over all frequencies, in practice a large percentage is still located in a small frequency range. In numerical simulation in the configuration of the analytical's solution $\tilde{b}_{G,a}$, we adjusted β to 100 because we observe that 95% of the total potential energy is selected as waves around a small bandwith of frequencies. This 95% value are kept for all the simulation of the Green's function from equation (2.3). To choose a lower β mean that less potential energy from equation (2.3) would be considered as waves, meaning that some eddies would be set as waves. On the contrary choosing, a higher β would not change much in the wave energy in equation (2.3) and might increase the number of eddies associated to IGW. In configurations other than the analytical solution, simulations of Green's functions also show that more or less 95% of the total potential energy is preserved as waves.

Then, the ζ filter is applied to the $\hat{u}^t, \hat{u}^p, \hat{b}$ fields extracted every $\Delta t'$ from the stationary part of the first type of DNS, *i.e.* over the same T period of extraction of VSHF. The inverse FFT then yields the decomposition (2.8). No Hann window is used to avoid modifying the signal and energy, except for the creation of ζ. All following statistics are averaged over $T_0 = 600\Delta t'$ in the middle of the time domain T. They do not change significantly if T_0 is halved, ensuring they are converged. All frequencies are adequately resolved since the minimum frequency is $\omega_{\min} = 2\pi/T$ and the maximum frequency is $\omega_{\max} = \pi/\Delta t'$. In supplementary material, the video compares the fields b, b^w, b^e for $N = 70$.

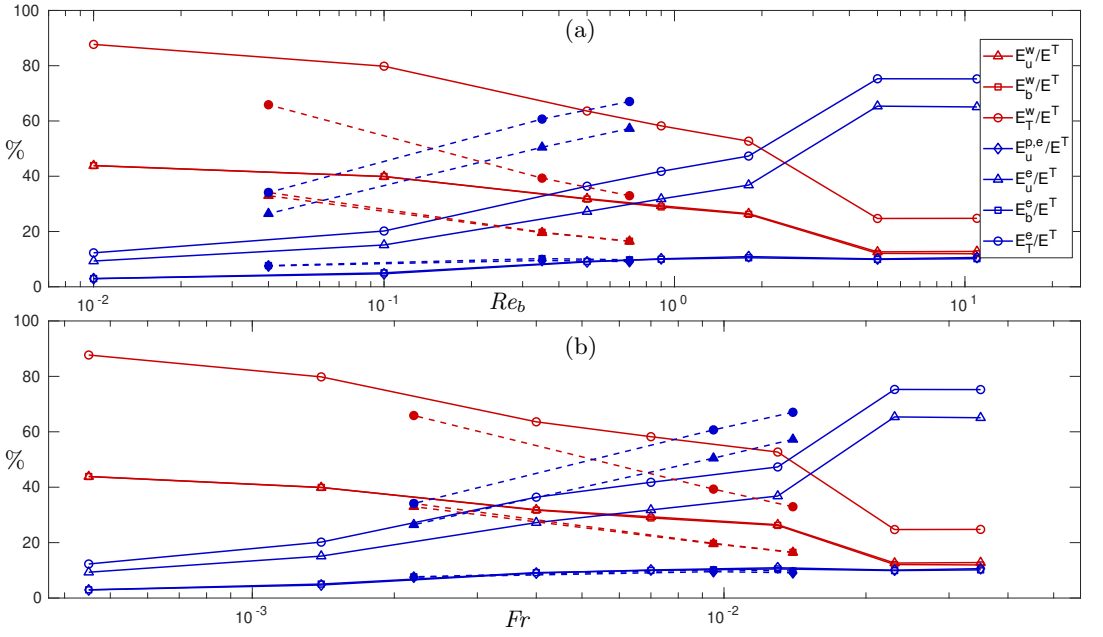

Figure 2: Evolution with Re_b of the percentage of energy in waves and eddies $(E_i^e/E^T, E_i^w/E^T)$ for kinetic, potential and total energy $(i = b, u, T$ respectively) against (a) Re_b (b) Fr. Numerical simulations with 512^3 points have empty symbols with solid line and numerical simulations with 256^3 points have filled symbols with dotted line.

4. Balance of energy between waves and eddies

4.1. *Energy of waves and eddies*

The total mechanical energy $E^T = E_u^T + E_b^T$ is the sum of kinetic energy E_u^T and potential energy E_b^T. Based on our orthogonal decomposition, we split these energies into their wave and eddy parts as $E^T = E^w + E^e$ and $E^l = E_u^l + E_b^l$, with $E_u^l = 0.5 < \hat{\mathbf{u}}^l, \hat{\mathbf{u}}^l >$ and $E_b^l = 0.5N^{-2} < \hat{b}^l, \hat{b}^l >$ where l stands for w (wave), e (eddy) or T (total) and $<,>$ is defined in section 2. The eddy part of the poloidal kinetic energy is defined as $E^{p,e} = 0.5 < \hat{\mathbf{u}}^{p,e}, \hat{\mathbf{u}}^{p,e} >$. Figure 2a and 2b shows for both resolution, the energy distribution between waves and eddies, E^e and E^w compare to total energy E^T. Since two parameters Fr and Re_b appear to be strongly correlated (i.e. $Re_b = Re_h Fr^2$), we plot the distribution against Fr and Re_b separately. Moreover, we can have an idea of the evolution of these energies either by fixing Re_b and weakly increasing Fr (from high to low resolution on figure 2a) or fixing Fr and weakly decreasing Re_b (from high to low resolution on figure 2b). As expected, on figure 2a, we observe that, the eddy part of any form of energy E^e increases, and the wave part E^w decreases when Re_b increases (figure 2a) and when Fr increases (figure 2b). Staquet & Godeferd (1998) found a similar distribution of kinetic energy (60% to eddies and 40% to waves) at $Fr \simeq 0.006$ for decaying turbulence. Moreover, at a fixed Re_b (figure 2a), when Fr increases, there is more energy in the eddy part than in the wave part which is expected by the meaning of Fr (inertia effects are more important than gravity effects). By increasing Fr, the evolution of E^w, E^e as a function of Re_b seems to be shifted to smaller values of Re_b as well as towards the equilibrium point i.e. the point where

$E^w = E^e$. Nevertheless, at a fixed Fr (figure 2b), when Re_b decreases, there is more energy in the eddy part than in the wave part which is not obvious. Once again, this evolution seems to be shifted towards a smaller value of Fr.

To analyse this result, we must analyse the composition of each type of energy. The figure 2a and 2b show the ratio of potential and kinetic energy distribution of waves (E_b^w, E_u^w) and eddies (E_b^e, E_u^e) compare to total energy E^T. First, we observe that the buoyancy energy E_b^w and kinetic energy E_u^w have the same percentage of total energy of waves i.e. $E_b^w \sim E_u^w$ for any Re_b or any Fr as expected from the characteristic of IGW. Secondly, we observe that the buoyancy energy of eddies is less than kinetic energy of eddies i.e. $E_u^e > E_b^e$ for any Fr or Re_b. Nevertheless, at fixed Fr, for example at $Fr \sim 0.014$, when Re_b decrease there is more kinetic energy in eddy for lower Re_b i.e. $E_u^e(Fr = 0.014, Re_b = 0.7) > E_u^e(Fr = 0.013, Re_b = 1.8)$. This non obvious result can be analysed by decomposing the kinetic energy of eddies into poloidal part and torodial part. By following the decomposition (2.7) and (2.8), the eddy part can be decomposed into poloidal and toroidal components: $E_u^e = E_u^{p,e} + E_u^{t,e}$ where $E_u^{p,e} = 0.5 < \hat{\mathbf{u}}^e \cdot \mathbf{e^p}, \hat{\mathbf{u}}^e \cdot \mathbf{e^p} >$ and $E_u^{t,e} = 0.5 < \hat{\mathbf{u}}^e \cdot \mathbf{e^t}, \hat{\mathbf{u}}^e \cdot \mathbf{e^t} >$. On figure 2a and 2b we have only plot the value of $E_u^{p,e}$ and the value of $E_u^{t,e} = E_u^e - E_u^{p,e}$ can be deduced. We observe the same percentage of total energy in the poloidal and buoyancy eddy energy, i.e. $E_b^e \sim E_u^{p,e}$ independently of Fr or Re_b. This percentage increases slowly with Re_b or with Fr. Note that total potential energy $E_b^T = E_b^w + E_b^e$ is linked to the available potential energy (see section 14.1 in Davidson (2013)). The available potential energy is a mechanical form of gravitational potential energy that stores the energy of an unstable density pattern i.e. the light and heavy density are not in equilibrium state. While a part of this unstable configuration is related to the IGW (E_b^w) as the waves induce spatial variations of density fluctuation, the other part (E_b^e) contain, among other things, the density overturn (light density over heavy density). It seems that the equality $E_b^e \sim E_u^{p,e}$ reflects the effect of eddies in the vertical plane, which is directly related to the poloidal part of the velocity field. Since $E_b^e \sim E_u^{p,e}$ is more or less constant with Re_b at a fixed Fr, this means that only the toroidal part $E_u^{t,e}$ increases when Re_b decreases. The increase of the toroidal part $E_u^{t,e}$ lead to an increase of the total kinetic energy of the eddy part E_u^t. We remind that the toroidal part $(k_h \neq 0)$ do not include the VSHF $(k_h = 0)$. Fabien : c est ici que c est un peu tendu, de defendre que c est le vortical mode grande echelle qui croit quand Re_b augmente. Generally, large scale dominated the kinetic energy in contrast to small scale dominated the dissipation, this means that the large scale vortical mode are well represented by the toroidal part of energy. This vortical mode can be associated with an increase in large, smooth and stable horizontal layers as we go deeper in the VASF regime by decreasing Re_b as indicated by Brethouwer *et al.* (2007). This observation could explain the shift of the distribution of energy E^w, E^e towards a smaller Fr as Re_b decreases.

Note that at very large Re_b, it seems that $E_u^{p,e} \sim E_b^e \sim E_b^w \sim E_u^w$. In the pure Riley's decomposition, at large Re_b, all the potential energy of the eddies E_b^e and the poloidal part of kinetic energy of eddies $E_u^{p,e}$ are defined to the wave part (i.e. $\sim 10\%$ for each part) that induce a difference of 40% in comparison to our results ($+20\%$ of energy in IGW and -20% of energy in eddies).

4.2. *Flux of waves and eddies*

The evolution of total energy in stratified turbulence is driven by the flux of energy in equation $dE^T/dt = P - \varepsilon_T$ where the total dissipation $\varepsilon_T = \varepsilon_u + \varepsilon_b$

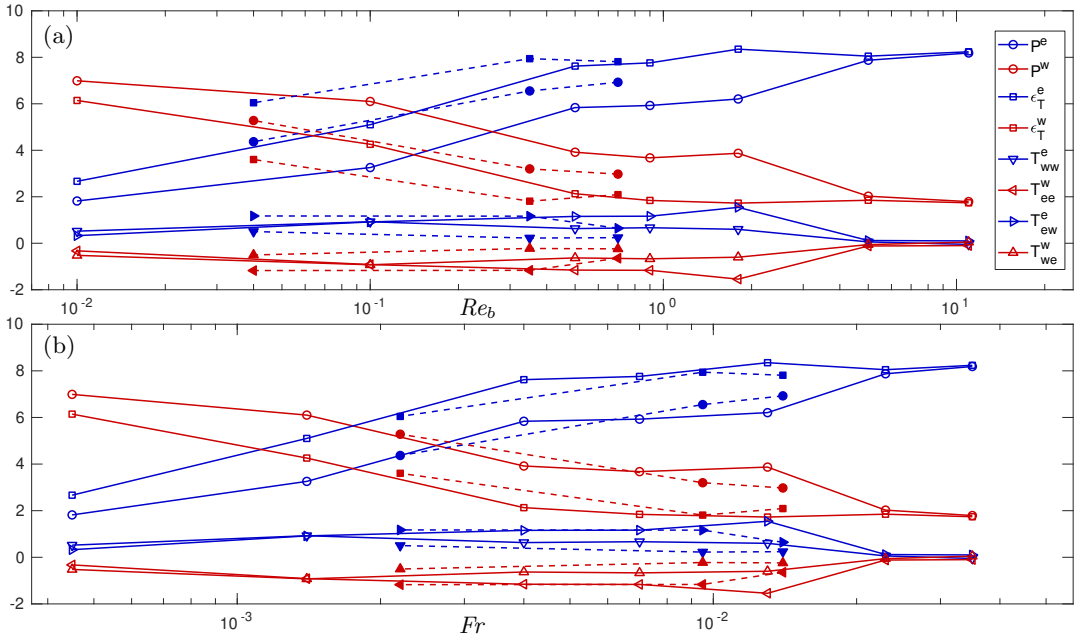

Figure 3: Evolution with (a) Re_b (b) Fr of the contributions of forcing P^l, dissipation ε^l and transfer T^l_{ij} for waves ($l = w$) and eddies ($l = e$). Numerical simulations with 512^3 points have empty symbols with solid line and numerical simulations with 256^3 points have filled symbols with dotted line.

with $\varepsilon_u = \nu < k^2\hat{\mathbf{u}}, \hat{\mathbf{u}} >$ and $\varepsilon_b = \mathcal{X}N^{-2} < k^2\hat{b}, \hat{b} >$. During the statistically stationary regime, the total energy stored is constant, so that $dE^T/dt = 0$ and, for all stratification intensities, the output flux balances the input flux as $P \simeq \varepsilon_T$. The wave and eddy decomposition now permits to address the question about how do wave- and eddy-related fluxes evolve with stratification? We consider the equation of evolution of wave and eddy parts described by Verma (2019) as Lin-type equations, and hence that for total energy. We start with equations $\widehat{(2.1)}$ and $\widehat{(2.2)}$ as space Fourier-transformed (2.1) and (2.2). We also use the space-Fourier-transformed decomposition of velocity and density (2.8), and we project both equations $\widehat{(2.1)}$ and $\widehat{(2.2)}$ on the wave part using the inner products $[\widehat{(2.1)}, \hat{\mathbf{u}}^w(\mathbf{k}, t)]$ and $[\widehat{(2.2)}, \hat{b}^w(\mathbf{k}, t)]$, and on the eddy part using $[\widehat{(2.1)}, \hat{\mathbf{u}}^e(\mathbf{k}, t)]$, and $[\widehat{(2.2)}, \hat{b}^e(\mathbf{k}, t)]$ relying on orthogonality properties noted in section 2. This yields four $(\mathbf{k}, t)$-dependent equations for potential/kinetic energy and for the wave/eddy part. Balance equations are finally obtained by summing the potential and kinetic energy and using the spectral integration $<,>$:

$$\begin{aligned} dE^w/dt &= T^w_{ee} + T^w_{we} + \varepsilon^w_T + P^w \\ dE^e/dt &= T^e_{ww} + T^e_{ew} + \varepsilon^e_T + P^e \end{aligned} \tag{4.1}$$

where $\varepsilon^l_T = \varepsilon^l_u + \varepsilon^l_b$ with $\varepsilon^l_u = \nu < k^2\hat{\mathbf{u}}^l, \hat{\mathbf{u}}^l >$ and $\varepsilon^l_b = \mathcal{X}N^{-2} < k^2\hat{b}^l, \hat{b}^l >$ is the total dissipation rate for each part $l = w, e$, the exchange term $T^l_{ij} =< \widehat{\mathbf{u}^i \times \boldsymbol{\omega}^j}, \hat{\mathbf{u}}^l > -N^{-2} < \widehat{\mathbf{u}^i \cdot \nabla b^j}, \hat{b}^l >$ and the injected power $P = P^w + P^e = 10$

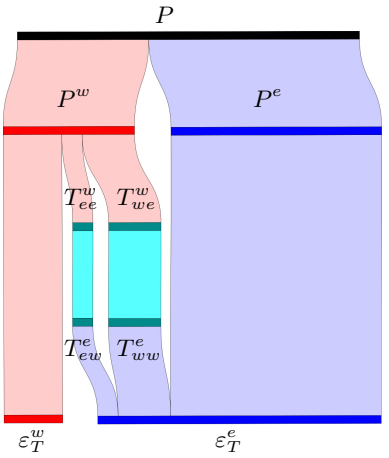

Figure 4: Sankey's diagram of energy flux at $Re_b = 1.8$ and $Fr = 0.013$ (see text).

for each part $P^l =< \hat{\mathbf{F}}_\mathbf{u}, \hat{\mathbf{u}}^l >$. In equations (4.1), one neglects the interactions T^l_{sj} of waves and eddies with VSHF because in our simulations these terms are small compared to others (for $N = 100$, $T^l_{sj} \sim \mathcal{O}(10^{-7} T^l_{ij})$). As discussed by Verma (2019), triadic transfers are such that $T^l_{ij} = -T^j_{il}$ so that $T^w_{we} = -T^e_{ww}$ and $T^e_{ew} = -T^w_{ee}$. T^l_{ij} is an energy exchange term between l and j parts, due to the interaction between the part j "convected" by part i that exchanges energy with part l. Thus, $T^j_{ij} = 0$ so that such terms are not net exchange terms, but are dynamically similar to convection terms, since they convey the modification of part j by part i that acts onto part j. For instance, $T^e_{ee} = 0$ and $T^w_{ww} = 0$ are respectively similar to a classical non-linear transfer between eddies and to a non-linear transfer between waves. In the statistically stationary regime, $dE^{w,e}_T/dt = 0$ and the equilibrium of the fluxes is reached since all terms compensate one another.

Figure 3a and 3b shows for both resolution, the evolution with Re_b and with Fr of the amount of the different terms in equation (4.1). Again, we can have an idea of the evolution of these values either by fixing Re_b and weakly increasing Fr (from high to low resolution) or fixing Fr and weakly decreasing Re_b (from high to low resolution). In order to facilitate physical interpretation, we show a corresponding flux diagram (a.k.a. Sankey's diagram) in figure 4 for $Re_b = 1.8$ and $Fr = 0.013$ to visualize quantitatively the energy flux from the injection P to the two dissipations ε^w_T and ε^e_T, either directly, or indirectly by wave/eddy exchange terms T^l_{ij}. Each bar represents a component of the balance of energy, with a width proportional to the energy flux it involves. Red, blue and cyan respectively indicate the wave, eddy and exchange parts.

Figure 3a and 3b shows that at $Re_b > Re^T_b \simeq 2$ and $Fr > Fr^T \simeq 0.02$, the input power for waves and eddies is in balance exclusively with the dissipation, i.e. $P^e \simeq \varepsilon^e_T$ and $P^w \simeq \varepsilon^w_T$ and there is no exchange between waves and eddies. This does not means that there is no transfer between waves and eddies, it only means that in overall, no transfer occur, but a scale by scale transfer (a "cascade") is still possible between them. However, this cascade is outside the scope of this article. Moreover, injected energy is mainly pumped by eddies since $P^e > P^w$. This changes completely when Re_b decreases or Fr decreases as $Re_b < Re^T_b$ or

$Fr < Fr^T$. Indeed, in the most stratified case $Fr = 0.00045$ at low $Re_b = 0.01$, the input power and dissipation are more important for the wave part than for the eddy part ($P^w > P^e$ and $\varepsilon_T^w > \varepsilon_T^e$) and the exchange terms T_{we}^w and T_{ee}^w remove energy from waves ($P^w > \varepsilon_T^w$) and redistribute it to eddies ($P^e < \varepsilon_T^e$). As Re_b increases and Fr increases close to the transition $Re_b \sim Re_b^T$ and $Fr = Fr^T$, the dissipation associated with eddies gets larger ($\varepsilon_T^e > \varepsilon_T^w$) as expected but, surprisingly, the input power for waves remains large and there is a significant transfer from the wave part to the eddy part which amounts to a total 25% of the eddy dissipation. During this transition, the exchange between wave and eddy is dominant. Similarly, in Godeferd & Cambon (1994), a lot of the energy appears to be pumped from the waves by the exchange term T_{we}^w. In this transition zone, at fixed Re_b, when Fr increases, as expected, the eddy part take more importance and the evolution seem to be shifted to a lower Re_b^T. Nevertheless, at a fixed Fr, when Re_b decreases, it seems that the evolution is still always the same and depends only on Fr, except perhaps the amplitudes. There is no obvious shifting.

These observations result in a global analysis of transfers between waves and eddies. Nevertheless, the global exchange is zero for the exchange terms, i.e. $T_{ee}^e = T_{ww}^w = T_{ew}^w = T_{we}^e = 0$. But these terms are associated to the "cascades" and therefore influence indirectly the transfers between wave and eddies. For example, the global term $T_{ew}^w = 0$ means that there is no global exchange, but there is a scale-by-scale transfer (a "cascade") between waves aided by an eddy that acts as a mediator (Verma 2019). The analysis of these terms requires a scale-by-scale examination to provide a better understanding of the internal mechanisms of energy transfer and cascade of energy. Nevertheless, this is outside of the scope of this article.

Furthermore the analysis is done here with a forcing that does not discriminate the partition of energy between waves and eddies. As a result, the dissipation terms are close to the energy input of the waves and eddies.

5. Mixing by waves or eddies

This wave/eddy flow decomposition permits to understand the contribution of IGW and eddies to mixing. The total mixing coefficient is defined by $\Gamma = \varepsilon_b/\varepsilon_u$ (Peltier & Caulfield 2003). For oceanographic application, the eddy diffusity of density κ_ρ can be used for parameterizing the stratification mixing with equation $\kappa_\rho = \mathcal{X} Pr \Gamma Re_b$ (Caulfield 2021). In this formulation, it is possible that a highly efficient mixing at low Re_b lead to a smaller eddy diffusity of density than flows with a higher Re_b. Γ is also useful for calculating the vertical diffusivity of density used in the model proposed by Osborn (1980). Whereas Γ was approximated to a constant $\Gamma \simeq 0.2$ in the ocean where $Re_b \sim 100 - 1000$ (Mashayek *et al.* 2017), recent DNS in decaying stratified turbulence at resolution 512^3 (Garanaik & Venayagamoorthy 2019) and forced stratified DNS at larger resolution (Maffioli *et al.* 2016), suggest a dependence of Γ with Fr and Re_b. On figure 5b, we have reported their values of Γ in a Froude range similar to ours, *i.e.* $Fr \ll 1$ and associated with $Re_b \simeq 10 - 20$ (forced case) and $Re_b \simeq 1 - 10$ (decaying case). Moreover, in a wave regime of superposed low-amplitude IGW with weak nonlinear interactions, Le Reun *et al.* (2018) find that $\Gamma = 1/Pr = 1$. Our simulations explore the transition between these two regimes. In order to understand separately the effect of waves and eddies on mixing, we therefore separate the total mixing coefficient $\Gamma = \Gamma^w + \Gamma^e$ into mixing due to waves

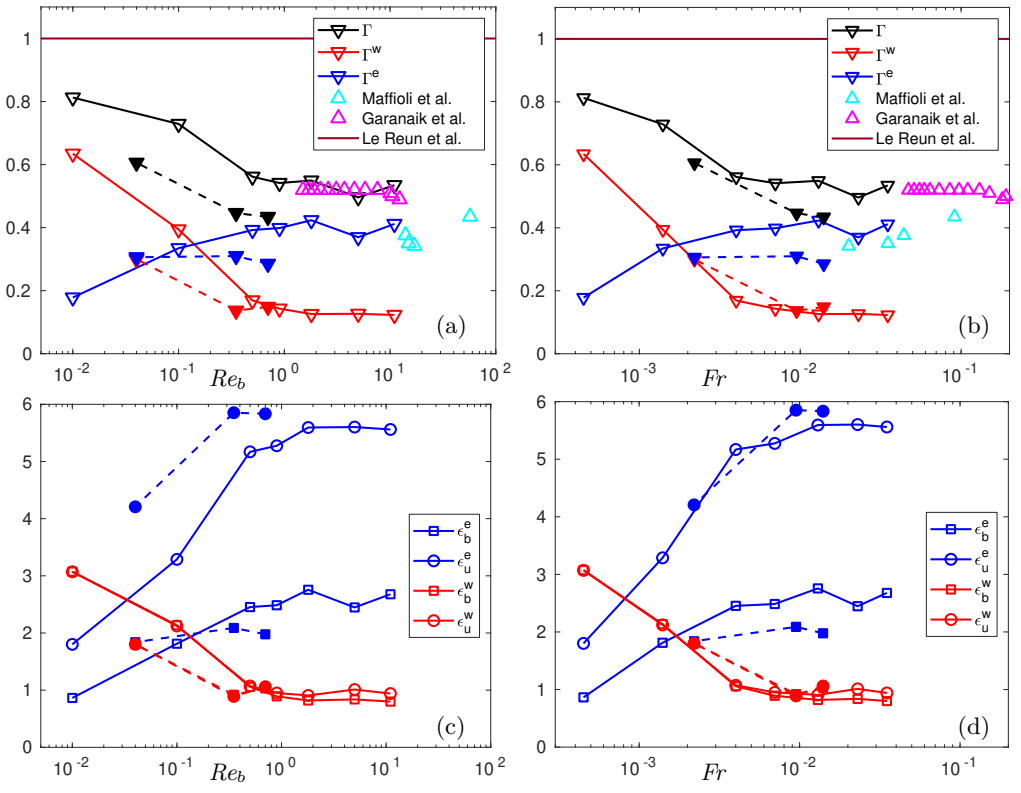

Figure 5: Mixing coefficients Γ, Γ^w, Γ^e compared with data from literature against (a) Re_b. (b) Fr. Kinetic and buoyancy dissipation for waves and eddies against (c) Re_b. (d) Fr. Numerical simulations with 512^3 points have empty symbols with solid line and numerical simulations with 256^3 points have filled symbols with dotted line.

$\Gamma^w = \varepsilon_b^w/(\varepsilon_u^e + \varepsilon_u^w)$ and mixing due to eddies $\Gamma^e = \varepsilon_b^e/(\varepsilon_u^e + \varepsilon_u^w)$ by using $\varepsilon_u = \varepsilon_u^e + \varepsilon_u^w$ and $\varepsilon_b = \varepsilon_b^e + \varepsilon_b^w$. On figure 5a and 5b, the coefficients Γ, Γ^w, Γ^e are reported in function separately of Re_b and Fr, and compared to the above-mentioned data. At first view, our coefficient values seem to coincide better with a variation in Fr rather than a variation in Re_b (as in the flux analysis, see previous section). For $Re_b \geqslant 1$ and $Fr \geqslant 10^{-2}$, we find similar value of $\Gamma \simeq 0.5$ as in Garanaik & Venayagamoorthy (2019) with similar resolution and slightly lower Froude number. Moreover, we observe that the wave mixing and eddy mixing reach a plateau, as expected, but the eddies mix more than waves i.e. $\Gamma^e \simeq 0.4 \geqslant \Gamma^w \simeq 0.1$. Note that our decomposition considers as eddies, among others, the breaking of internal waves or overturning with vertical velocity. This could nuance the belief that overturning is the main source of mixing (Gregg *et al.* 2003). The global mixing coefficient found by Maffioli *et al.* (2016) is close to our mixing coefficient by eddies Γ^e. As their DNS are done at a higher $Re_b \simeq 10-20$, it is possible that their flows contain mostly eddies, resulting in a mixing coefficient dependent only on mixing by eddies. When $Re_b \to 0$, the total mixing increases and tends to $\Gamma \simeq 1$ as expected by Le Reun *et al.* (2018). In this case, Γ^w increases a lot, whereas Γ^e decreases. Indeed, we expect at very low buoyancy Reynolds number that the waves dominate the flow and become the main factor

of mixing. At fixed Fr, when Re_b decreases, the same physics is shifted to low Re_b but in a non-obvious way the plateau value seems to be constant for wave mixing $\Gamma^w \simeq 0.1$ while mixing by eddy seem to be weaker $\Gamma^e \simeq 0.3$.

In order to better understand the physical phenomena underlying mixing and its modelling, an in-depth analysis of the different dissipation terms is necessary. Note that while kinetic and buoyancy energy are more related to large scales, the different dissipations are related to small scales. On Figure 5c and 5d, we have plotted the different terms of dissipation as function of Re_b and Fr. Note that during statistically stationary regime, the constant forcing $P = 10$ and dissipation are in balance i.e. $P \simeq \varepsilon_u^e + \varepsilon_u^w + \varepsilon_b^e + \varepsilon_b^w$. First, as expected for IGW, the kinetic and potential dissipation of the waves are equal, i.e. $\varepsilon_b^w \sim \varepsilon_u^w$. Moreover, this confirms the idea proposed by Le Reun *et al.* (2018) that $\Gamma = 1$ is always true for the IGW even if they are mixed with eddies. Secondly, the kinetic dissipation of eddies is greater than the potential dissipation of eddies i.e. $\varepsilon_u^e > \varepsilon_b^e$. Thirdly, all these values tend towards a plateau when Fr is large and $Re_b \simeq 1$ where $\varepsilon_b^w \sim \varepsilon_u^w \sim \varepsilon_u^e/6$. This plateau involves a plateau for mixing. At first view, our coefficient values seem to coincide better with a variation in Fr rather than a variation in Re_b which shift the evolution to a lower Re_b. At a fixed Fr, as Re_b decreases, all dissipation terms remain unchanged except ε_b^e, which implies that the mixing due to the eddy Γ^e decreases.

6. Conclusion and Perspectives

We have developed and used an extension of the Riley's decomposition (Riley *et al.* 1981) to separate waves and eddies in a stratified flow. This method takes into account the vertical mixing and the temporal/spatial properties of waves with their modifications by the mean flow (VSHF). We apply this analysis on DNS results with strong stratification ($Fr \leqslant 1$), but varying buoyancy Reynolds number over a wide range of regimes, from a viscously affected stratified regime ($Re_b \ll 1$) to stably stratified turbulence regime ($Re_b \gg 1$). From this separation, as expected, we show that the total wave energy dominates for $Re_b \ll 1$ and the total eddy energy dominates for $Re_b \gg 1$. There is an equipartition in the wave energy between the kinetic and the potential part which indicates that we succeeded in obtaining a good extraction of the IGW in the turbulent mixing for any Re_b. Moreover, for a large Re_b, the potential energy of eddies has a value similar to those of the potential or kinetic energy of waves. Moreover, we establish the balance equations of energies separately for wave and eddy parts. In a statistically stationary regime, the different fluxes of the energy balance are studied from input forcing to output dissipation and by taking into account the exchange between parts. We observe that dissipation by eddies is more efficient than dissipation by waves except at largest stratification. This higher efficiency comes from an exchange that pumps the energy from the wave part and sends it to the eddy part, where it is dissipated. This scenario seems valid from low turbulence at $Re_b \ll 1$ to higher turbulence at $Re_b \sim 1$. Moreover, the dissipation of kinetic energy and potential energy have the same value, which means that the characteristics of IGW are well captured by our method. Beyond this, at $Re_b \gg 1$, the input power is directly dissipated by each part separately, with no global exchange. However, the study of transfer by waves and eddies with themselves will require further scale-by-scale analysis in order to identify their specific contributions to the turbulent cascade. Our analysis also provides

access to dissipation, and therefore to the contributions of waves and eddies to the mixing coefficient Γ. A result particularly relevant for mixing models is the plateau reached at high buoyancy Reynolds number Re_b by split mixing contributions, showing that eddy mixing is four times that of waves for our higher resolution. However, it would be relevant to explore higher resolution results in order to obtain Γ^w and Γ^e values at a much higher Re_b while keeping the Fr small. We assumed $Pr = 1$, nevertheless, as shown by (Smyth *et al.* 2001), the Prandtl number can have a large effect on the mixing comparing to other possible Prandtl number, especially when comparing with ocean mixing. Moreover, we have used a constant power forcing that does not discriminate between the wave and eddy part, so the interaction between these two parts is decisive. Nevertheless, it would be interesting to use different types of forcing in order to influence more or less the interaction between waves and eddies.

Funding. This research was funded by `ANR DisET` grant number `ANR-17-CE30-0003`. This work was granted access to the HPC resources of `IDRIS` under the allocation `A0062A02206` made by `GENCI` and HPC ressources of the `FLMSN`, partner of `EQUIPEX EQUIP@MESO`.

Declaration of interests. The authors report no conflict of interest.

Author ORCID. H. Lam, https://orcid.org/0000-0002-2604-2714; F. S. Godeferd, https://orcid.org/0000-0002-8898-5451

REFERENCES

Bartello, P. 1995 Geostrophic adjustment and inverse cascades in rotating stratified turbulence. *J. Atmos. Sci.* **52** (24), 4410–4428.

Brethouwer, G., Billant, P., Lindborg, E. & Chomaz, J.-M. 2007 Scaling analysis and simulation of strongly stratified turbulent flows. *J. Fluid Mech.* **585**, 343–368.

Caulfield, C.P. 2021 Layering, instabilities, and mixing in turbulent stratified flows. *Annual Review of Fluid Mechanics* **53** (1), 113–145.

Davidson, Peter Alan 2013 *Turbulence in rotating, stratified and electrically conducting fluids*. Cambridge University Press.

Di Leoni, P. C., Cobelli, P. J. & Mininni, P. D. 2015 The spatio-temporal spectrum of turbulent flows. *The European Physical Journal E* **38** (136).

Di Leoni, P. C. & Mininni, P. D. 2015 Absorption of waves by large-scale winds in stratified turbulence. *Phys. Rev. E* **91** (3), 033015.

Garanaik, A. & Venayagamoorthy, S. K. 2019 On the inference of the state of turbulence and mixing efficiency in stably stratified flows. *J. Fluid. Mech.* **867**, 323–333.

Godeferd, F. S. & Cambon, C. 1994 Detailed investigation of energy transfers in homogeneous stratified turbulence. *Phys. Fluids* **6** (6), 2084–2100.

Gregg, M. C., Sanford, T. B. & Winkel, D. P. 2003 Reduced mixing from the breaking of internal waves in equatorial waters. *Nature* **422** (6931), 513–515.

Herbert, C., Marino, R., Rosenberg, D. & Pouquet, A. 2016 Waves and vortices in the inverse cascade regime of stratified turbulence with or without rotation. *J. Fluid. Mech.* **806**, 165–204.

Ivey, G.N., Winters, K.B. & Koseff, J.R. 2008 Density stratification, turbulence, but how much mixing? *Annual Review of Fluid Mechanics* **40** (1), 169–184, arXiv: https://doi.org/10.1146/annurev.fluid.39.050905.110314.

Kimura, Y. & Herring, J. R. 2012 Energy spectra of stably stratified turbulence. *J. Fluid. Mech.* **698**, 19–50.

Lam, H., Delache, A. & Godeferd, F. S. 2020 Partitioning Waves and Eddies in Stably Stratified Turbulence. *Atmosphere* **11** (4), 420.

Le Reun, T., Favier, B., Barker, A. J. & Le Bars, M. 2017 Inertial wave turbulence driven by elliptical instability. *Phys. Rev. Let.* **119** (3).

Le Reun, T., Favier, B. & Le Bars, M. 2018 Parametric instability and wave turbulence driven by tidal excitation of internal waves. *J. Fluid. Mech.* **840**, 498–529.

Lelong, M.-P. & Riley, J. J. 1991 Internal wave–vortical mode interactions in strongly stratified flows. *J. Fluid. Mech.* **232**, 1–19.

Lindborg, E. & Brethouwer, G. 2007 Stratified turbulence forced in rotational and divergent modes. *J. Fluid. Mech.* **586**, 83.

Lvov, Yuri V, Polzin, Kurt L, Tabak, Esteban G & Yokoyama, Naoto 2010 Oceanic internal-wave field: theory of scale-invariant spectra. *J. Phys. Ocean.* **40** (12), 2605–2623.

MacKinnon, J. A. et al. 2017 Climate Process Team on Internal Wave–Driven Ocean Mixing. *Bull. Am. Meteo. Soc.* **98** (11), 2429–2454.

Maffioli, A., Brethouwer, G. & Lindborg, E. 2016 Mixing efficiency in stratified turbulence. *J. Fluid. Mech.* **794**, R3.

Maffioli, Andrea, Davidson, PA, Dalziel, SB & Swaminathan, Nedunchezhian 2014 The evolution of a stratified turbulent cloud. *Journal of fluid mechanics* **739**, 229.

Maffioli, A., Delache, A. & Godeferd, F. S. 2020 Signature and energetics of internal gravity waves in stratified turbulence. *Phys. Rev. Fluids* **5**, 114802.

Mashayek, A., Salehipour, H., Bouffard, D., Caulfield, C. P., Ferrari, R., Nikurashin, M., Peltier, W. R. & Smyth, W. D. 2017 Efficiency of turbulent mixing in the abyssal ocean circulation. *Geophys. Res. Let.* **44** (12), 6296–6306.

Moulin, F. & Flór, J.-B. 2006 Vortex–wave interaction in a rotating stratified fluid: Wkb simulations. *J. Fluid. Mech.* **563**, 199–222.

Müller, P. 1976 On the diffusion of momentum and mass by internal gravity waves. *J. Fluid. Mech.* **77** (4), 789–823.

Müller, Peter, Holloway, Greg, Henyey, Frank & Pomphrey, Neil 1986 Nonlinear interactions among internal gravity waves. *Rev. Geophys.* **24** (3), 493–536.

Olbers, Dirk J 1976 Nonlinear energy transfer and the energy balance of the internal wave field in the deep ocean. *J. Fluid. Mech.* **74** (2), 375–399.

Osborn, T. R. 1980 Estimates of the Local Rate of Vertical Diffusion from Dissipation Measurements. *J. Phys. Oceano.* **10** (1), 83–89.

Peltier, W. R. & Caulfield, C. P. 2003 Mixing efficiency in stratified shear flows. *Ann. Rev. Fluid Mech.* **35** (1), 135–167.

Riley, J. J., Metcalfe, R. W. & Weissman, M. A. 1981 Direct numerical simulations of homogeneous turbulence in density-stratified fluids **76** (1), 79–112.

Savaro, C., Campagne, A., Linares, M. C., Augier, P., Sommeria, J., Valran, T., Viboud, S. & Mordant, N. 2020 Generation of weakly nonlinear turbulence of internal gravity waves in the Coriolis facility. *Phys. Rev. Fluids* **5**, 073801.

Smith, Leslie M & Waleffe, Fabian 1999 Transfer of energy to two-dimensional large scales in forced, rotating three-dimensional turbulence. *Physics of fluids* **11** (6), 1608–1622.

Smith, L. M. & Waleffe, F. 2002 Generation of slow large scales in forced rotating stratified turbulence. *J. Fluid. Mech.* **451**, 145–168.

Smyth, W. D., Moum, J. N. & Caldwell, D. R. 2001 The efficiency of mixing in turbulent patches: Inferences from direct simulations and microstructure observations. *Journal of Physical Oceanography* **31** (8), 1969 – 1992.

Staquet, C. & Godeferd, F. S. 1998 Statistical modelling and DNS of decaying stably stratified turbulence. Part 1. flow energetics. *J. Fluid. Mech.* **360**, 295–340.

Verma, M. K. 2019 *Energy Transfers in Fluid Flows: Multiscale and Spectral Perspectives*. Cambridge University Press.

Waite, Michael L & Bartello, Peter 2004 Stratified turbulence dominated by vortical motion. *Journal of Fluid Mechanics* **517**, 281.